Chemical Pathways in the Interactions of Reactive Metal Atoms with Organic Surfaces: Vapor Deposition of Ca and Ti on a Methoxy-Terminated Alkanethiolate Monolayer on Au

A. V. Walker,*,† T. B. Tighe,‡ B. C. Haynie, S. Uppili, N. Winograd,* and D. L. Allara*

Department of Chemistry and The Materials Research Institute, Pennsylvania State University, University Park, Pennsylvania 16802

Received: February 5, 2005; In Final Form: April 14, 2005

In situ time-of-flight secondary ion mass spectrometry, infrared spectroscopy, and X-ray photoelectron spectroscopy measurements have been used to characterize the interfacial chemistry that occurs upon physical vapor deposition of Ti and Ca atoms onto a $-OCH_3$ terminated alkanethiolate self-assembled monolayer (SAM) on Au{111}. While the final result for both metals is near-exhaustive degradation of the methoxy terminal group and partial degradation of the alkyl chains to inorganic products such as carbides, hydrides, and oxides, the reaction mechanisms differ significantly. Titanium reacts in parallel with the $-OCH_3$ and $-CH_2-$ units, extensively degrading the latter until a metallic overlayer forms preventing further degradation. At this point, there is a cessation of the Ti−SAM reactions. In contrast, Ca is initially consumed by the $-OCH_3$ terminal group via a reaction mechanism involving two $-OCH_3$ groups; subsequent depositions lead to alkyl chain degradation, but at a rate slower than that for Ti deposition. These results demonstrate the subtle differences in chemistry that can arise in the vapor deposition of reactive metals, and have important implications for the behavior of electrical interfaces in organic and molecular devices made with Ti or Ca top contacts.

1. Introduction

The vacuum deposition of metal layers on organic thin films is a widely used process with many technological applications from barrier coatings to electronic devices. In all these applications, the ability to control the performance of these metal-organic composite structures is greatly aided by a fundamental understanding of the mechanisms of the metal atom−organic interaction. To facilitate the unraveling of these complex phenomena, recent efforts have focused on using the chemical variability and well-defined structures of self-assembled monolayers (SAMs) in fundamental studies involving vapor-deposited metal films.[1−8] An impetus for these studies is also provided by recent developments in molecular electronic devices[9−29] for which the nature of vapor-deposited top metal contacts in SAM-based devices can be a significant issue.[11]

A wide range of behaviors and mechanisms are possible when metal atom vapors impinge on SAMs and, in general, on organic substrates.[1−8] In the case of metals with no chemical affinity for the organic matrix, the eventual character of the interface is solely determined by the initial competition among metal atom nucleation to form clusters with discontinuous morphologies, uniform wetting of the surface, and penetration into the organic matrix.[4−8] In the case of highly reactive metal atoms, the resulting structural features can be quite complex, ranging from a sharp interfacial layer of chemically bonded metal to a severely degraded organic substrate with formation of inorganic phases, such as a metal oxides or carbides. Here the specific chemistry of the metal atoms with the organic moieties (or "functional groups") will be a major factor in driving the various reaction pathways.[8]

In a previous study of the vapor deposition of Al atoms onto a methoxy group-terminated hexadecanethiolate SAM on Au{111}, $H_3CO(CH_2)_{16}S-$/Au, we observed that under ambient temperature conditions no chemical reaction occurred between the $-OCH_3$ group and the Al.[5] Rather, a weak complexation or solvation interaction was observed. This is striking in view of the thermolytic stability of the oxide, carbide, and hydride compounds of Al[30] and the availability of O, C, and H atoms at the surface of the SAM. Indeed, density functional theory (DFT) calculations showed that reactions of isolated Al atoms with the $-OCH_3$ group in the SAM molecules are thermochemically exothermic by considerable energies. For example, insertion of an Al atom into either C−O bond of the $-CH_2-O-CH_3$ moiety is 263 kJ/mol exothermic.[5] It was concluded that subtle steric effects at the SAM surface together with inaccessibly high activation energies for bond insertion override the thermochemical driving forces under the deposition conditions.

Since both kinetic and thermodynamic driving forces affect the interaction of Al atoms with SAMs, we were interested in determining how other reactive types of metal atoms behave at SAM surfaces. To normalize the comparisons, the $H_3CO-(CH_2)_{16}S-$/Au SAM was chosen as a common substrate. The metals Ti and Ca were chosen since both metals also form thermolytically stable oxides, carbides, and hydrides, like Al.[30] As a further motivation to study Ca deposition, both Al and Ca are used as top contacts in organic electronic devices because of their low work functions.[31,32] Calcium is also a common contact for poly(*p*-phenylenevinylene) (PPV)-based light-emitting diodes.[33]

* To whom correspondence should be addressed. D.L.A.: phone, (814) 863-2254; fax, (814) 863-0618; e-mail, dla3@psu.edu. N.W.: phone, (814) 863-0001; fax, (814) 863-0618; e-mail, nxw@psu.edu. A.V.W.: phone, (314) 935-8496; fax, (314) 935-4481; e-mail, walker@ wustl.edu.

† Present address: Department of Chemistry, Campus Box 1134, Washington University, St. Louis, MO 63130.

‡ Present address: Motorola Laboratories, 2100 Elliot Road, Tempe, AZ 85284.

10.1021/jp0506484 CCC: $30.25
Published on Web 05/14/2005

Salaneck and co-workers have observed that vapor-deposited Ca diffuses into the near surface region (2−3 nm) of both α,ω-diphenyltetradecaheptaene[34] and poly(2,5-diheptyl-*p*-phenylenevinylene)[35] films with donation of electrons to the polymer π system to form Ca^{2+} ions. These authors also noted that for these PPV-type surfaces with oxygen-containing species an interfacial layer of calcium oxide forms. The inclusion of Ti was motivated also by its wide use in Si-based microelectronic applications,[36,37] and its recent use in molecule-based electronic switches[12,16,17,27,28] and diodes.[9,20,23] Pointing to the aggressive nature of Ti, reports have demonstrated that vapor-deposited Ti reacts indiscriminately with triazine, polyimide, polystyrene, polyethylene, and epoxy films to form Ti−O, Ti−C, and Ti−N bonds,[36−40] and with fluoropolymers forming Ti−C, Ti−O, and Ti−F bonds.[41] Konstadinidis and co-workers have also examined the interaction of Ti with $-CO_2H$-, $-CO_2CH_3$-, $-CH_3$-, −OH-, and −CN-terminated alkanethiolate SAMs[42] and concluded that Ti−O bonds are formed with the ester- and alcohol-terminated SAMs, Ti−N bonds with the nitrile group, and Ti−C bonds with all the SAMs that were studied. At low metal coverages, the metal atoms reacted with the terminal functional groups, while at higher coverages, bonds were formed directly with the $-CH_2-$ units of the SAM. Furthermore, it appeared that in the initial stages of deposition the Ti overlayer did not grow layer by layer but rather formed clusters on the SAM surface.

In this paper, we show through time-of-flight secondary ion mass spectrometry (TOF SIMS), infrared spectroscopy (IRS), and X-ray photoelectron spectroscopy (XPS) measurements how vapor-deposited Ca and Ti interact with a $-OCH_3$ terminated SAM. The results reveal that both Ca and Ti react vigorously with the SAM to form M−O and M−C bonds, where M represents the deposited metal, in marked contrast to the previous case of Al for which no reactions occur under the same deposition conditions. Deposited Ti aggressively reacts with both the terminal $-OCH_3$ group and the alkyl chain $-CH_2-$ units to degrade the SAM in a top down fashion toward the S/Au interface. In contrast, Ca reacts first with the $-OCH_3$ group followed by degradation of the alkyl chain, but at a significantly slower rate than for Ti. These results show the dramatic differences in reactivities for these generally reactive metals and point to the importance of considering the underlying chemistry when designing metal−molecule contacts in organic or molecular electronic devices.

2. Experimental Section

2.1. Materials and General Procedures. The preparation and characterization of the $H_3CO(CH_2)_{16}S-$/Au SAM has been described in detail previously[5,43−48] and is summarized briefly here. Sequential thermal depositions of Cr (∼10 nm) and Au (∼200 nm) were made onto clean Si(001) native oxide-covered wafers. Self-assembly of well-organized monolayers was achieved by immersing the Au substrates in millimolar solutions of the relevant alkanethiol molecules in absolute ethanol for ∼2 days at ambient temperature. The monolayer films were characterized with single-wavelength ellipsometry, infrared spectroscopy, and contact angle measurements to ensure that they were densely packed, clean surfaces. In some cases, tapping mode AFM images (Dimension Series 3000, Digital Instruments, Santa Barbara, CA) were obtained to verify the quality of the starting Au/Cr substrate surfaces (typically, 1.0−1.3 nm rms roughness) and the subsequent SAMs (no change from substrate roughness). In addition, all SAMs were characterized by the initial TOF SIMS and IRS measurements prior to metal deposition.

The purity of the Ca and Ti employed (Goodfellow, Alfa Aesar, Sigma Aldrich) was ≥99.99%. Metals were deposited onto a room temperature sample using resistively heated tungsten baskets at a rate of ∼0.15 atom nm^{-2} s^{-1}. The source−sample distance was >30 cm, and the sample temperatures remained near ∼25 °C. The deposited mass of metal was monitored using a quartz crystal microbalance (QCM)[49] (TOF SIMS, Maxtek Inc. TM-400, maximum error of ±8%; IRS and XPS, Sigma Instruments SQM-160, maximum error of ±7%).

2.2. Time-of-Flight Secondary Ion Mass Spectrometry. The TOF SIMS analyses were performed on a custom-designed instrument as described previously.[50] Briefly, the instrument consists of a loadlock, a preparation chamber, a metal deposition chamber, and the primary analysis chamber, each separated by a gate valve. The primary Ga^+ ions were accelerated to 15 keV and contained in a 100 nm diameter probe beam which was rastered over a 106 μm × 106 μm area during data acquisition. All spectra were acquired using a total ion dose of less than 10^{11} ions cm^{-2}. Relative peak intensities can be reproduced within ±8% from sample to sample and ±8% from scan to scan.

During deposition, the pressure remained $<5 \times 10^{-8}$ Torr. After deposition, the preparation chamber pressure was allowed to recover to the base value of 1.5×10^{-9} Torr before the sample was transferred to the analysis chamber.

2.3. Infrared Spectroscopy. Analyses were performed on a Fourier transform instrument (Mattson Research Series 1000) fitted with custom in-house optics configured external to the instrument and designed for grazing incidence reflection of samples under vacuum.[3−8] A liquid nitrogen-cooled MCT detector was used with an effective low-frequency cutoff of ∼750 cm^{-1}. The infrared beam passed through the analysis chamber through a pair of differentially pumped KBr windows. After analysis of the bare monolayer, a shield was moved to unblock the path between the sample and the metal source. The pressure remained $<3 \times 10^{-7}$ Torr during the deposition. The final spectra were determined as $-\log(R/R_o)$, where R is the sample spectrum and R_o is the reference spectrum of a bare gold wafer or a $C_{16}D_{33}S$/Au{111} SAM. The latter primarily was used as the reference, except for samples in which the reference spectral features overlapped sample features of interest. In these cases, a rigorously cleaned Au sample served as the reference.

2.4. X-ray Photoelectron Spectroscopy (XPS). The XPS analyses were performed using a Kratos Analytical Axis Ultra apparatus equipped with a monochromatic Al Kα source operating at an X-ray power of 280 W. Spectra were collected at a 90° photoelectron takeoff angle with respect to the sample plane with a pass energy of 20 eV and an energy step of 0.15 eV. The resulting fwhm of the Au $4f_{7/2}$ line was 0.71 eV. All spectra were referenced to the Au $4f_{7/2}$ line at 84.0 eV. Following analysis of the uncoated monolayer, the samples were transferred under a continuous vacuum to the deposition chamber, which was isolated from the analysis chamber by a gate valve. During the depositions, the pressure remained $<1 \times 10^{-7}$ and $<1 \times 10^{-8}$ Torr for Ca and Ti, respectively. After deposition, the metal/SAM specimen was transferred directly in vacuo back to the analysis chamber where the pressure was maintained below 5×10^{-9} Torr.

2.5. Definition and Measurement of Deposited Metal Coverage. The metal deposition onto the samples was monitored directly as the mass per unit area, ρ_A (23.1 atoms nm^{-3} for Ca and 56.7 atoms nm^{-3} for Ti), by a QCM. For ease in data analysis, the deposited amounts were converted to coverage of

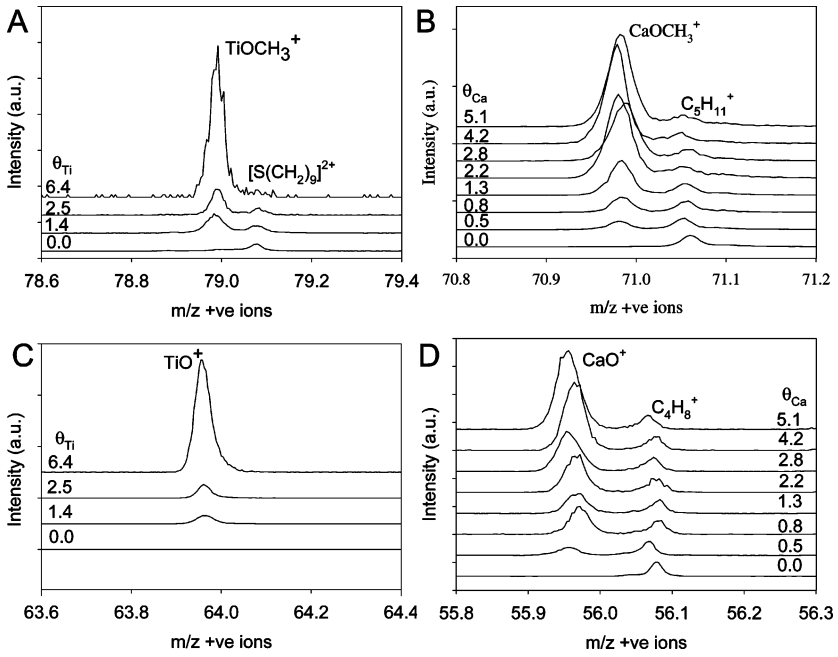

Figure 1. High-resolution SIMS spectral overlays from the $-OCH_3$ SAM. The spectra show the progression of metal−organic fragments with Ti and Ca deposition. Panels A−D represent positive ions with nominal masses of 79, 71, 64, and 56 amu, respectively. The intensities in panels A−D are normalized to the initial peak intensities of $[S(CH_2)_9]^{2+}$, $C_5H_{11}^+$, Au^+, and $C_4H_8^+$, respectively.

metal atoms per SAM molecule (θ_M, M = Ti or Ca) using the ρ_A and a molecular density of 4.6 molecules nm^{-2} for a well-formed alkanethiolate/Au{111} SAM.[46] Thus, when $\theta_M = 1$, there will be on average one metal atom deposited per SAM molecule.

3. Results

3.1. TOF SIMS. A detailed discussion of the positive and negative ion mass spectra of the bare $-OCH_3$ monolayer is given in ref 5. In agreement with previous work,[3−5,51−54] we find that the relative intensities of Au_X^-, $Au_XS_Y^-$, and SO_Z^- (where $Z = 1-4$) provide us with a useful indication that the SAM was prepared without substantial incorporation of impurities or oxidative products.

3.1.1. Reaction with the $-OCH_3$ Group. In the positive ion mass spectrum, upon deposition of Ti or Ca on the $-OCH_3$ SAM, we observe the formation of the $MOCH_3^+$ and MO^+ ions where M = Ca or Ti. In Figure 1, the $TiOCH_3^+$, TiO^+, $CaOCH_3^+$, and CaO^+ spectra are normalized to the initial peak intensities of $[S(CH_2)_9]^{2+}$, Au^+, $C_5H_{11}^+$, and $C_4H_8^+$, respectively, to make obvious the changing peak intensities with respect to the hydrocarbon and substrate fragments as the deposition progresses. On the basis of our previous work with $-COOH$[4] and $-CO_2CH_3$,[3] the appearance of MO^+ indicates that the deposited metal, Ca or Ti, has undergone a redox reaction with the methoxy functionality to form M−O bonds.

There are, however, some important differences between Ca and Ti. Upon deposition of Ca, the formation of $CaO_2C_2H_5^+$ ions is observed (Figure 2), suggesting that Ca interacts with two adjoining methoxy-terminated alkanethiolate moieties.

3.1.2. Penetration of Metal Atoms into the SAM and Reaction with the $-CH_2-$ Chain. The observation of ions containing both M and S indicates that the deposited metal atoms have penetrated through the $-OCH_3$-terminated SAM to the S/Au interfacial region, where the formation of the mixed cluster peaks becomes possible.[3,5] In Figure 3, high-resolution positive ion mass spectra of MSH_2^+ (M = Ti or Ca) are displayed. The $TiSH_2^+$ and $CaSH_2^+$ ion intensities are normalized to $C_6H_{10}^+$ and $[S(CH_2)_3]^+$, respectively. For both metals, we note that the observed increase in MSH_2^+ ion intensity is slower than for the MO^+ or $MOCH_3^+$ ion intensity, and suggests that the first increments of deposited atoms react preferentially with the terminal group with subsequent reaction and penetration into the chain interior and the S/Au interface region.

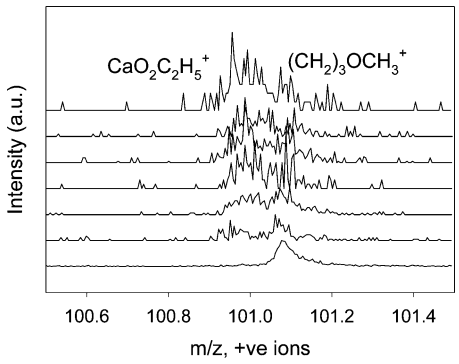

Figure 2. High-resolution SIMS spectral overlays from the $-OCH_3$ SAM upon deposition of Ca, which represents positive ions with a nominal mass of 101 amu. The spectra are normalized to the initial peak intensities of $(CH_2)_5OCH_3^+$ to make obvious the changing peak intensities with respect to the hydrocarbon fragment as the deposition progresses.

We can further examine the state of the penetrated and interacting Ti or Ca atoms by studying the M_x^+ signals, where M = Ti or Ca (Figure 4). With the first increment of deposited Ti or Ca, monomer, dimer, M_2^+, and trimer, M_3^+, intensities increase in a parallel fashion. In our previous work with Al, we demonstrated that these signals differ between the case where deposited Al chemisorbs at the $-OCH_3$ terminus and the case where it penetrates through the monolayer to the S/Au interface.[3,4] Following this interpretation, the early growth of M_2^+ intensity in our case supports the conclusion that some fraction of the metal atoms penetrate to the Au/S interface region. Given the reactivity of the metal atoms, it is likely that the mechanism involves initial rapid degradation in some areas of the SAM which leads to metal atoms penetrating close to the Au substrate surface.[5]

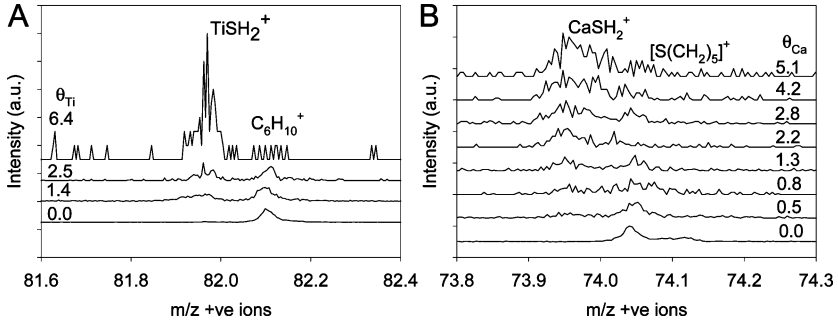

Figure 3. High-resolution SIMS spectral overlays from the OCH_3 SAM. The spectra show the progression of metal−organic fragments with Ti and Ca deposition. Panels A and B show spectra for positive ions with nominal masses of 82 and 74 amu, respectively. The intensities in plots A and B are normalized to the initial peak intensities of $C_6H_{10}^+$ and $[S(CH_2)_5]^+$, respectively.

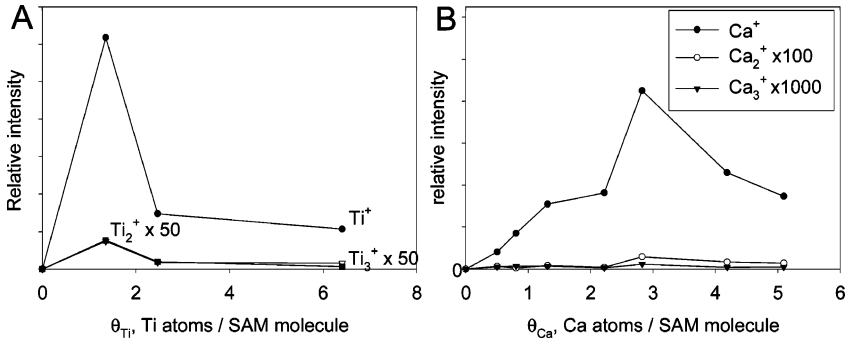

Figure 4. Integrated SIMS ion peak areas plotted vs θ_M for the OCH_3 SAM. Panel A shows the peak areas of Ti_n^+ ($n = 1-3$) vs θ_{Ti}, and panel B shows the peak areas of Ca_n^+ ($n = 1-3$) vs θ_{Ca}.

In contrast to the previously reported inertness of Al atoms with hydrocarbon groups,[3−5] we note that the deposited Ti and Ca atoms react with the methylene backbone. Upon Al deposition, the $(CH_2)_{16}H^+$ ion intensity rapidly decreases to a constant, non-zero value (Figure 5a), consistent with no reaction of the alkyl chain. In contrast, for both Ti and Ca depositions, the $(CH_2)_{16}H^+$ ion intensity (Figure 5) decreases and approaches zero with increasing metal coverage, an indication that the deposited Ca or Ti reacts with the methylene backbone. A further indication that the deposited metal atoms react with the backbone is that AuM^+ (M = Ti or Ca) fragments are observed (Figure 6). These ions would appear only from regions where the SAM molecules had been severely degraded or even removed. No such signals would be observed if the metal atoms exclusively reacted with the terminal group[3−5] or penetrated to the Au/S interface with no reaction.[3,5−8]

3.1.3. Formation of Metal Carbide Products. Finally, upon deposition of Ca or Ti atoms, we observe that CaC^+, CaC_2^+, and TiC^+ peaks form and increase in intensity with further increments of metal atom deposition (Figure 7). The CaC^+, CaC_2^+, and TiC^+ intensities are normalized to the peak intensities of $C_4H_4^+$, $C_5H_4^+$, and $C_2H_5S^+$, respectively, to make obvious the changes in peak intensity as the deposition progresses. This observation would be consistent with the formation of metal carbide types of products. No MC_n^+ signals are observed for metals which do not react with the $-CH_2-$ units (e.g., Al).[3,5−8]

3.2. IRS. The previously reported assignments[5,47,55,56] of the main peaks of the bare monolayer (Figures 8 and 9; $\theta_M = 0$) are summarized briefly for reference: 1132, 1390, and 1465 cm^{-1} are the C−O−C antisymmetric stretch ($\nu_{C\text{-}O}$), the $-CH_3$ symmetric deformation (δ_{CH_3}), and the $-CH_2-$ scissor deformation (δ_{CH_2}), respectively; 2851 and 2918 cm^{-1} are the $-CH_2-$ symmetric C−H stretch (d^+) and the $-CH_2-$ antisymmetric C−H stretch (d^-) modes, respectively; and 2811, 2828, 2931,

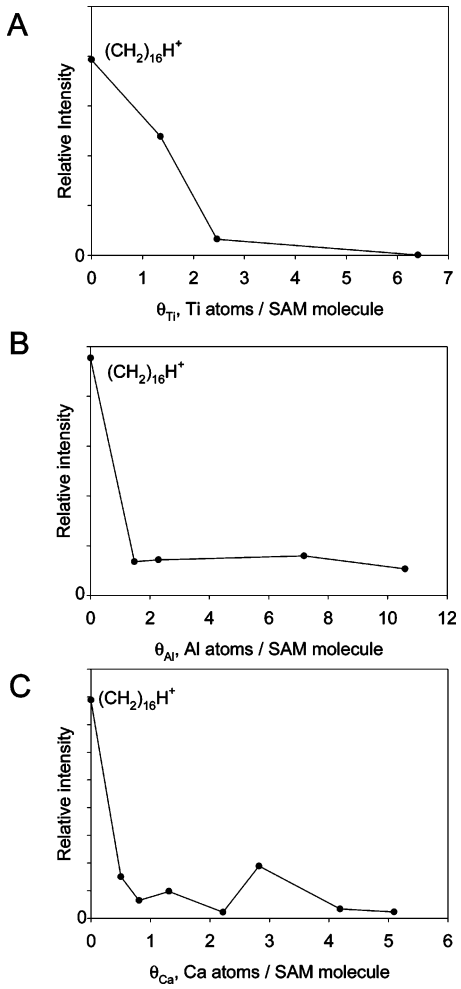

Figure 5. SIMS peak intensity of $(CH_2)_{16}H^+$ with Ti (A), Al (B), and Ca (C) deposition.

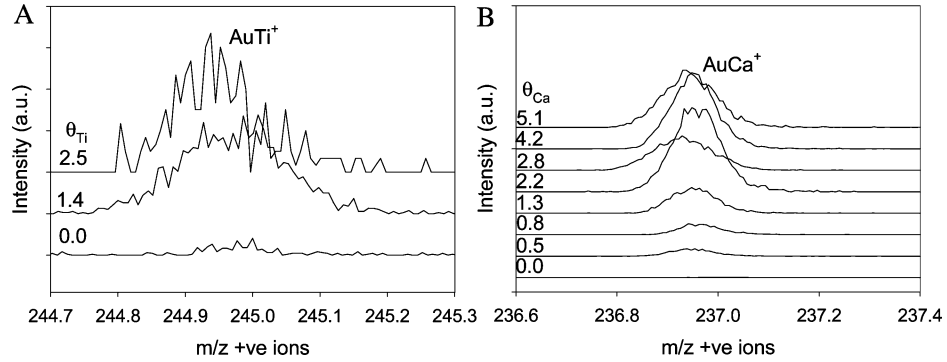

Figure 6. High-resolution SIMS spectral overlays from the $-OCH_3$ SAM. The spectra show the progression of metal−organic fragments with Ti and Ca deposition. Panels A and B show spectra for positive ions with nominal masses of 245 and 237 amu, respectively.

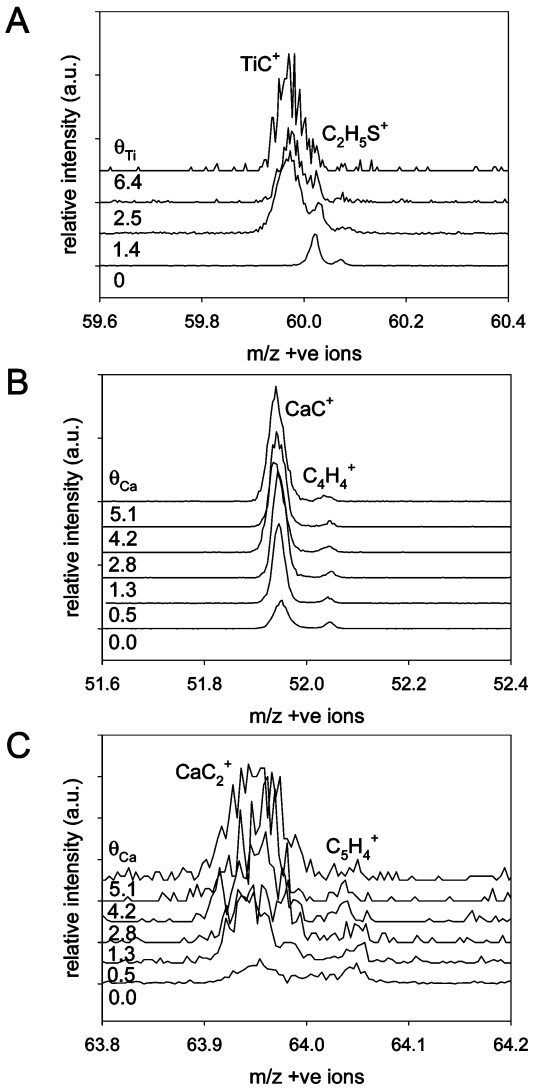

Figure 7. High-resolution SIMS spectral overlays of positve ions with nominal masses of 60 (A), 52 (B), and 64 amu (C). The spectra are normalized to the initial peak intensities of $C_2H_5S^+$, $C_4H_4^+$, and $C_5H_4^+$, respectively.

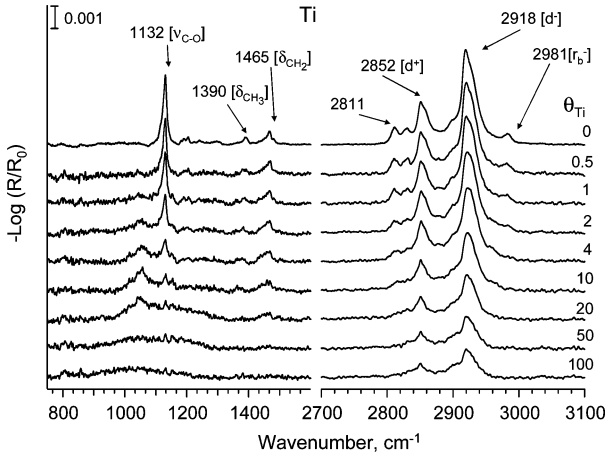

Figure 8. IRS spectra as a function of Ti coverage for deposition on the $-OCH_3$ SAM. The main diagnostic peaks are indicated by arrows with the frequencies and assignments for the bare SAM.

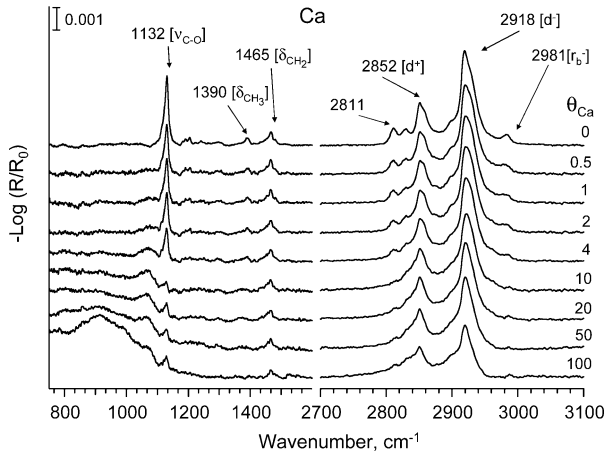

Figure 9. IRS spectra as a function of Ca coverage for deposition on the $-OCH_3$ SAM. The main diagnostic peaks are indicated by arrows with the frequencies and assignments for the bare SAM.

and 2981 cm^{-1} are the various C−H stretching modes of the CH_3 group (defined collectively as ν_{CH_3}).

3.2.1. Reaction with the $-OCH_3$ Group. The aggressive chemical degradation of the $-OCH_3$ group by both Ti and Ca is shown by the rapid attenuation of the $\nu_{C\text{-}O}$, δ_{CH_3}, and ν_{CH_3} intensities for increasing metal coverage (Figures 8 and 9). The trends of the relative integrated peak intensities of $\nu_{C\text{-}O}$, δ_{CH_3}, and d^- versus coverage (Figure 10) are consistent with attack at both the C−O and C−H bonds. The $\nu_{C\text{-}O}$ intensity plots show that the reaction is essentially complete when $\theta_{Ti} \sim 50$ and $\theta_{Ca} \sim 20$, while the δ_{CH_3} intensity plots indicate completion when $\theta_{Ti} \sim 3$ and $\theta_{Ca} \sim 10$. Comparison of the initial slopes of the δ_{CH_3} and ν_C-O mode integrated intensity plots for both metals indicates that three metal atoms react with one $-OCH_3$ group, suggesting that M−C, M−H, and M−O bonds form, where M = Ti or Ca. We note that the stoichiometry for the reaction of Ti or Ca with $-OCH_3$ to form thermochemically stable species TiC, TiH_2, and TiO_2 or CaC_2, CaH_2, and CaO is 3:1 (Ti:$-OCH_3$ or Ca:$-OCH_3$).[30] However, we have no direct evidence for these specific products.

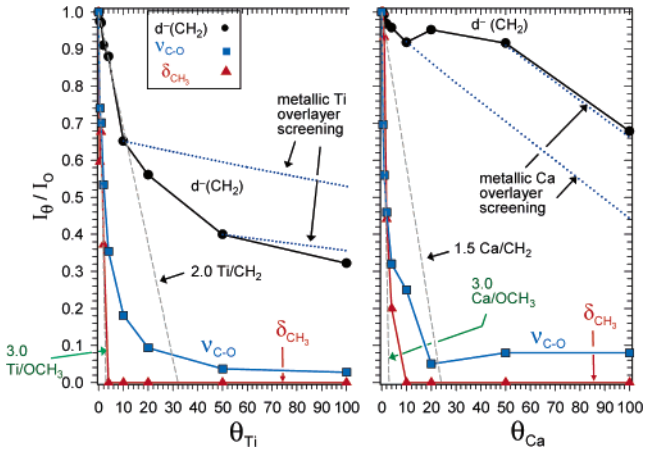

Figure 10. Metal coverage dependence of the integrated peak intensities from Figures 8 and 9 for the C−H antisymmetric stretch (d^-) (black ●), the C−O stretch (ν_{CO}) (blue ■), and the CH_3 bend (δ_{CH_3}) (red ▲) at 2918, 1132, and 1390 cm^{-1}, respectively, where I_θ/I_o is the integrated peak intensity (I_θ) at θ_M (M = Ti or Ca) divided by the integrated peak intensity for the bare SAM (I_o). Note that the OCH_3 IR peaks (ν_{CO} and δ_{CH_3}) decrease sharply with initial deposition of both metals, whereas the CH_2 peak (d^-) decreases far more slowly with an increase in θ_{Ca} than with θ_{Ti}. (- - -) Theoretical metal coverage dependence of I_θ/I_o for exhaustive degradation to the most stable inorganic products for each metal. Note that exhaustive degradation of CH_2 and OCH_3 groups appears to be followed for Ti up to $\theta \sim 20$ and 3−4, respectively. For Ca, the $-OCH_3$ group appears to undergo exhaustive degradation only when $\theta_{Ca} \leq 2$. (·····) Theoretical loss in IR intensity due to electric field screening that would result if all deposited metal formed a uniform metallic overlayer, starting at the coverage indicated at the beginning of each dotted line.

New peaks at 1000−1100 cm^{-1} (Figures 8 and 9) are assigned to species resulting from insertion of a metal atom into the C−O bond. When $\theta \sim 1-2$ for Ti and Ca, broad peaks arise, centered at ~1056 and 1070 cm^{-1}, respectively, and are assigned as $-(H_2C)-OX$ (X = a metal−organo species, e.g., Ti−CH_3) stretches of the species formed by insertion of a metal atom into the O−CH_3 bond.[57] This assignment is consistent with the observation of $MOCH_3^+$ and MO^+ ions in the TOF SIMS spectra (Figure 1). Upon further deposition of Ca, an intense, very broad peak centered at ~900 cm^{-1} appears (Figure 9) and is assigned as a Ca−O stretch, based on the approximate coincidence of the position with that expected for the LO mode of the Ca−O phonon of solid CaO.[58] After cessation of the Ca deposition, the magnitude of this peak slowly continues to increase. Upon completion of the metal deposition, several samples were left in vacuo; after 1 h, the intensity of the peak at ~900 cm^{-1} had nearly quadrupled. Since Ca is highly reactive with oxygen,[35,36] we attribute this additional growth to reaction with background oxygen in the vacuum system (base pressure of $\sim 5 \times 10^{-8}$ Torr) to form CaO at the surface. Overall, given the lack of information about the optical function spectra of the possible metal−organic and −inorganic species (oxides, carbides, and hydrides), it is not possible to quantify the various amounts of reaction product species.

3.2.2. Competition for Attack at $-CH_2-$ and $-OCH_3$ Units. Comparison of the variation of the ν_{C-O} and δ_{CH_3} intensities upon deposition with those of the d^- intensities shows that Ti is much less selective than Ca in reaction with the $-OCH_3$ terminal and $-CH_2-$ alkyl chain groups (Figure 10). For Ti deposition, when $\theta_{Ti} \leq 20$, the slope of the d^- intensity versus coverage indicates that two Ti atoms react with one $-CH_2-$ unit (Figure 10, dashed line), which suggests formation of both Ti−C and Ti−H bonds. This stoichiometry is consistent with the formation of TiC and TiH_2,[30] although we have no direct evidence for these products. These results, combined with the observation that Ti reacts nearly exhaustively with the $-OCH_3$ group, lead to a mechanism involving an initial indiscriminate reaction with the terminal $-OCH_3$ and the methylene chain ($-CH_2-$) groups. Ti deposits continue to attack the alkyl chain until further reaction is halted by formation of a metallic Ti overlayer. When $\theta_{Ti} \sim 20$, the reaction of deposited Ti with the terminal $-OCH_3$ groups is essentially complete while the $-CH_2-$ reaction continues. For example, when $\theta_{Ti} = 50$, the loss of the integrated d^- intensity indicates nearly 60% of the $-CH_2-$ alkyl chain groups have reacted. However, we note at these high coverages the loss of IR peak intensity can arise from both chemical reaction and electromagnetic screening by formation of metallic overlayers uniformly covering the SAM. Intensity losses in principle also could occur from additional tilting of the alkyl chains to a more compact layer, but this contribution is easily discounted on the basis that the SAM is already fully dense. To account for the electromagnetic screening factor, the dotted lines in Figure 10 display the theoretical screening losses for uniform Ti metal overlayer growth starting at $\theta_{Ti} = 10$ or at $\theta_{Ti} = 50$.[59] Note that when $\theta_{Ti} \geq 50$ the observed loss of d^- intensity nearly parallels the electromagnetic screening loss. From this, we conclude that when $\theta_{Ti} \geq 50$ the Ti−SAM reaction has essentially ceased and continued deposition results in formation of a metallic Ti overlayer which no longer contacts the SAM.

For Ca deposition, comparison of the variation of the ν_C-O and δ_{CH_3} integrated intensities with that of d^- clearly shows that Ca almost exclusively attacks the $-OCH_3$ terminal group (Figure 10). While reaction with the $-OCH_3$ group is almost complete when $\theta_{Ca} \sim 10$, only ~4% of the d^- intensity is lost; even when $\theta_{Ca} \sim 50$, there is an only ~8% loss of intensity. For a $-(CH_2)_{15}-$ alkyl chain, this is equivalent to a loss, on average, of ~1.2 $-CH_2-$ units per SAM molecule. While this observation suggests that Ca selectively reacts only with the terminal $-OCH_3$ group and the adjacent $-CH_2-$ unit, the theoretical electromagnetic screening loss seems to contradict this (Figure 10, dotted line). Between θ_{Ca} values of 10 and 50, the predicted screening loss of the d^- integrated intensity if a metallic overlayer exclusively were forming exceeds the experimentally observed loss. This strongly suggests that the Ca is not being deposited as a uniform metallic overlayer in this coverage region. Rather, a major fraction of the Ca instead is penetrating deep into the SAM and/or at the Au/S interface where it cannot effectively screen the IR absorption. Given the small decrease in the d^- intensity (~8%), presumably only a small fraction of this Ca reacts with the SAM, and the remainder of the deposited Ca is a metallic phase. These results indicate that the Ca is approaching the surface through deep (significant fraction of the SAM thickness), localized (perhaps molecular size scale) damage regions involving extensive degradation of a fraction of the alkyl chains in localized regions filled with Ca metal. When $\theta_{Ca} \geq 50$, however, the observed d^- intensity loss parallels the screening loss, indicating that a uniform metallic overlayer is forming with no further reaction with the SAM.

For both Ti and Ca, it is important to note that the average degree of conformational order of the remaining alkyl chains is largely unaffected. For example, note in Figures 8 and 9 that the position of the d^- remains close to 2918 cm^{-1}, indicating constant conformational order. This observation implies that attack at the $-OCH_3$ group, which occurs extensively in the initial deposition stages before significant numbers of $-CH_2-$ chain units have been attacked, does not induce any significant conformational disordering of the chains. It also suggests that

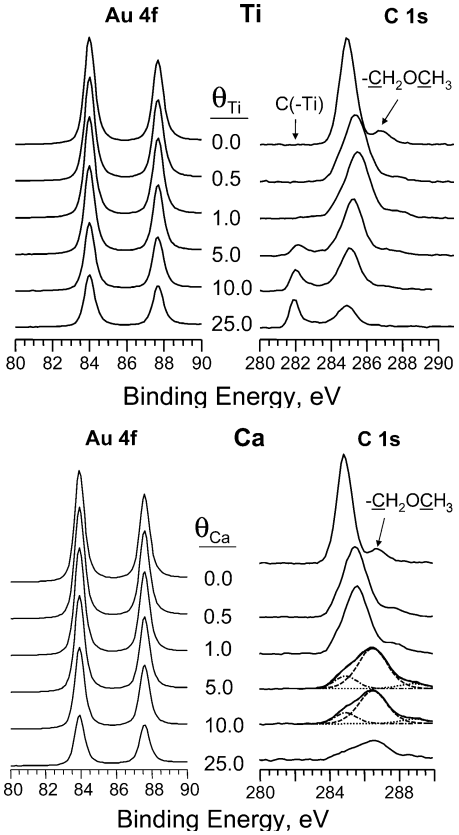

Figure 11. XPS spectra of the Au 4f and C 1s core levels for the deposition of Ti and Ca on the $-OCH_3$ SAM as a function of metal coverage. The data are shown with arbitrary intensities, with the correct relative intensity scales for each set of plots, and the C 1s binding energy positions set relative to the Au 4f peaks. For Ca deposition, the dashed spectra within the main peak envelopes of the C 1s spectra at $\theta_{Ca} = 5.0$ and 10.0 represent curve fits with three components, assigned in increasing order of binding energy, as a carbide species (as occurs in metal carbides), the $-CH_2-$ carbons, and a small residual $-CH_2-OCH_3$ feature. The carbide peak is shifted ~1.6 eV to a lower binding energy than the main $-CH_2-$ peak.

groups of alkyl chains are selectively removed by the deposited metal atoms, perhaps at SAM defect sites, while leaving chains in other regions intact, as opposed to a continuous degradation of all chains, which would be expected to cause serious perturbations of the d^- $-(CH_2)-$ antisymmetric stretching mode. This picture of selective, localized attack is consistent with a degradation mechanism involving localized, penetrating chemical damage of the SAM, as proposed above for Ca on the basis of the electromagnetic screening analysis.[60]

3.3. XPS. The objective of the XPS experiments was to provide further details of the inorganic reaction products from the Ti and Ca depositions. Data were collected for the Au 4f, C 1s, O 1s, S 2p, Ti 2p, and Ca 2p core levels. The O 1s (and Ti and Ca 2p) data were not useful for diagnostic purposes because there was significant interference from continuous background oxidation of the deposited metals during the experiment, especially Ca (also see IRS data in section 3.2.1) (data shown in Supporting Information). For the bare SAMs, the C 1s peaks (Figure 11) at binding energies (BEs) of 284.9 and 286.8 eV are assigned to the $-(\underline{C}H_2)-$ alkyl chain and the $-\underline{C}H_2O\underline{C}H_3$ C atoms, respectively. A single O 1s peak at 533.1 eV (data shown in Supporting Information) is assigned to $-CH_2\underline{O}CH_3$. These assignments are in good agreement with previous data.[5,37]

3.3.1. Formation of Carbide Products from Ti and Ca Deposition. The Au $4f_{7/2}$ spectra (Figure 11) show the expected monotonic decrease in peak intensity as the depositions proceed (~50% loss at $\theta_{Ti} = 25.0$ and ~65% at $\theta_{Ca} = 25.0$).[42,61] The constant line shape and positions for these peaks also indicate that there is negligible charging or alloying at the gold interface.

At low coverage, the C 1s region (Figure 11) shows initial reaction at the $-OCH_3$ group, in agreement with the TOF SIMS and IRS data. When $\theta = 0.5$, there is an ~50 and ~40% loss in the $-\underline{C}H_2O\underline{C}H_3$ peak area upon Ti and Ca deposition, respectively. The main $-(\underline{C}H_2)-$ peak broadens and has a positive BE shift. Continued deposition results in a steady decrease in both the $-\underline{C}H_2O\underline{C}H_3$ and $-(\underline{C}H_2)-$ peak intensities.[62] There are differences, however, in the observed C 1s peaks upon deposition of Ti and Ca. Between θ_{Ti} values of 1.0 and 5.0, a low BE peak appears at 282.1 eV and its relative intensity increases with increasing coverage. This peak is consistent with the formation of a species containing Ti−C types of bonds (i.e., a titanium carbide type of species).[42] When $\theta_{Ti} \geq 10.0$, deposited Ti becomes increasingly unreactive with or inaccessible to the remaining $-OCH_3$ moieties. When $\theta_{Ti} = 25.0$, there is a small residual $-\underline{C}H_2O\underline{C}H_3$ C 1s peak (~10% of the initial area). In contrast for Ca deposition, when $\theta_{Ca} = 5.0$ the $-\underline{C}H_2-$ C 1s peak starts to broaden very asymmetrically. For Ca deposition, when $\theta_{Ca} \geq 5.0$, the C 1s peak continues to shift to a higher BE with a low BE tail growing in. The low-BE C 1s feature can be approximately fitted by the presence of a new peak ~1.6 eV below the main $-CH_2-$ peak, which is consistent with the appearance of a carbide species.[63]

The O 1s, Ca 2p, and Ti $2p_{3/2}$ spectra are also consistent with the formation of O- and C-containing inorganic reaction products (see the Supporting Information). However, we cannot determine conclusively which species arise from reaction with the SAM and which from background gases (O_2, H_2O, etc.) (see the Supporting Information). The TOF SIMS data indicate that deposited Ti and Ca penetrate into the interior region of the SAM, close to the Au/S interface. However, we note that the S 2p spectra qualitatively appear to be unchanged upon metal deposition, indicating that there is not a significant amount of Ti or Ca penetrating and reacting with the thiolate S atoms. This is also consistent with the IRS data (see section 3.2.2) which suggest formation of a significant fraction of the metallic phases in the early stages of the metal phase growth occurs by deposition into localized pits of partially degraded chains in the SAM.

4. Discussion

For convenience in the following discussion, the overall reaction processes of the reaction of Ti and Ca with the $-OCH_3$ SAM are summarized in cartoon form in Figure 12. From the TOF SIMS, IRS, and XPS data, we conclude that under our deposition conditions Ca and Ti react with the C−O, C−H, and C−C bonds in the $-OCH_3$-terminated SAM to form a chemically and structurally complex inorganic composite. Indeed, the TOF SIMS and XPS data are consistent with the formation of titanium and calcium carbide.[64]

The IRS data also suggest that the stoichiometry of the reaction is consistent with the formation of TiC, TiH_2, and TiO_2 and CaC_2, CaH_2, and CaO with Ti and Ca deposition, respectively.

For both Ti and Ca deposition, the initial reactions occur at the terminal $-OCH_3$ group. When $\theta_M = 20-25$ (M = Ti or Ca), both the C 1s core level XPS peaks associated with the $-OCH_3$ group (Figure 11) and the IRS C−O stretch and $-CH_3$ deformation modes (Figures 8−10) have nearly vanished. Further, the IRS data suggest that three metal atoms react with

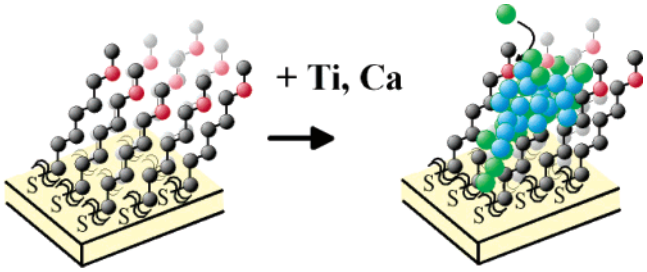

Figure 12. Cartoon showing a cross section of an $-OCH_3$ SAM sample, before sufficient metal deposition to produce a metallic phase, with selected important features of the reaction pathways of deposited Ti and Ca, as deduced from the experimental data. The metal atoms are colored green, oxygens red, and hydrocarbons black. The inorganic products (carbides, hydrides, and oxides) resulting from attack of the deposited metal atoms are colored blue. The picture is meant to indicate that degradation occurs in localized regions with penetration toward, but not completely to, the S/Au interface. Note that the localized degradation leaves some regions of alkyl chains (black) nearly intact, while other regions show severe degradation to residual inorganic products.

one methoxy group which is consistent with the formation of metal carbides (TiC and CaC_2), oxides (TiO_2 and CaO), and hydrides (TiH_2 and CaH_2). The TOF SIMS data are also consistent with this picture; $M_xO_y^{\pm}$ and $M_xC_y^{+}$ ions are seen to form (Figures 1 and 7). Finally, the IRS and XPS data indicate that a small fraction (5−10%; Figure 10) of these terminal methoxy groups never react with the deposited metal atoms.

The TOF SIMS data also indicate that deposited Ca selectively reacts with two methoxy groups (Figure 2) in preference to reactions with the methylene units of the alkyl backbone. There is no clear reason why deposited Ca would show a bidentate interaction with the terminal $-OCH_3$ groups while Ti would react with just one methoxy. One possible reason could involve steric effects. The average distance between adjacent methoxy groups in the SAM is fixed at ∼4.6 Å.[46] Comparison with the metallic diameters of 3.94 and 2.95 Å for Ca and Ti, respectively,[65] suggests that on space filling arguments alone Ca is more likely to interact with two-OCH_3 functional groups.

Both Ti and Ca react with the methylene units ($-CH_2-$) of the alkyl chains. Both the extent and mechanism of the reaction, however, are very different for each metal. For Ti deposition, reaction with the $-CH_2-$ groups occurs in parallel with the attack on the terminal $-OCH_3$ group and continues after reaction with the methoxy group is complete (Figures 8 and 10). The IRS data indicate that two Ti atoms react with one $-CH_2-$ unit, which is consistent with the formation stoichiometry of TiC and TiH_2. We note that the IRS data, however, indicate that the reaction nearly ceases by $\theta_{Ti} \sim 50$. At this point, subsequent deposition results in only a metallic phase. The ∼60% of the unreacted $-CH_2-$ groups remain unaffected by further deposition. In contrast, Ca nearly exclusively reacts with the $-OCH_3$ terminal group (Figure 10). By $\theta_{Ca} \sim 50$, Ca has only reacted with ∼8% of the methylene units, equivalent to ∼1.3 $-CH_2-$ groups of the C16 alkyl chain (Figure 10).

While the metal reactivity is important for both Ca and Ti deposition, the resultant metal−molecule morphology is controlled by the spatial aspects of the degradation process. There are two limiting cases for the kinetics of SAM degradation: (a) a gradual erosion of the SAM toward the Au/S interface and (b) a localized chemical damage mechanism in which the initial attack at a terminal group on the SAM leads to rapid removal of SAM molecules in the immediate local volume. The TOF SIMS data show strong evidence that the metal atoms penetrate deep toward the Au/S interface (Figures 1 and 6) which could be caused by either mechanism a or b. The IRS data (Figure 1), however, indicate that mechanism b is operative, especially for Ca deposition. One possible reason is that when a deposited Ca atom interacts with two terminal $-OCH_3$ groups further reaction with the methylene chain is blocked and a metallic overlayer forms instead. If a deposited Ca atom reacts with only one $-OCH_3$ group, however, the SAM can be degraded. Finally, the XPS S 2p data (see the Supporting Information) also support mechanism b since there appears to be no reaction between the deposited metal and the thiolate group. This suggests that metal atom penetration occurs in cavities in the SAM structure, as opposed to metal atom diffusion to the Au/S interface.[8]

If a localized, penetrating chemical damage mechanism were operative, one would expect the SAM surface to roughen and the deposited metal to cluster on the surface. To test this outcome, we performed tapping mode AFM on the $-OCH_3$ SAM surface before and after deposition at $\theta_M = 25$ (M = Ti or Ca). In both cases, we observe evidence for clustering of the metal atoms on the surface and a slight roughening of the surface (see the Supporting Information).

The $-OCH_3$ surface, with its relatively moderate reactivity and polarity, is one that is attractive for inducing uniform wetting of a deposited metal for a number of applications. On the basis of their thermochemistry, both Ti and Ca, as well as other reactive atoms such as Al, would be expected to all react vigorously and uniformly with the $-OCH_3$ surface to form stable carbide, oxide, and hydride products. The results presented here, however, as well as the previous ones on Al,[5] demonstrate wide differences in the characteristics of the depositions, ranging from immediate, selective chemical attack at the $-OCH_3$ groups with Ca to parallel attack at the $-OCH_3$ and $-CH_2-$ moieties with Ti and a lack of chemical attack with Al.[5] These results conclusively establish that the competition between kinetic and thermodynamic control is a key factor in determining the outcome of metallization processing for reactive metals. This in turn suggests that the detailed morphology and chemical pathways could be exquisitely controlled by changing the sample temperature and the metal atom kinetic energies. In particular, this approach should be useful for producing tailored metal−organic interfaces with important applications to technological areas such as metal−organic device contacts.

5. Conclusions

Upon deposition of Ti and Ca at controlled rates, the structure of the $-OCH_3$-terminated SAM layer is partially converted via attack at C−O, C−H, and C−C bonds to a complex structured inorganic composite of carbides, hydrides, and oxides intermingled with residual elements of the original SAM. The metal atoms both react vigorously with the SAM and penetrate toward the Au/S interface, predominantly in localized regions across the surface. In the case of titanium, the reactions with the $-OCH_3$ terminal group and the $-CH_2-$ alkyl chain units proceed in parallel. In contrast, vapor-deposited Ca reacts immediately with the terminal group followed by reaction with the alkyl chain units. These results provide an important background for understanding the underlying structural and chemical effects that arise in the formation of metal−organic interfaces in electronic applications such as the use of calcium or titanium for metallic contacts in PLEDs[33,34] and molecular electronic devices.[9,11,12,16,17,20,21,23−28] In these cases, for example, it is critical to be able to understand how the device properties will vary with the formation of inorganic interfacial phases and the nonuniformity of the chemical character of the device interface. More broadly, it is important to understand that the

outcome of the depositions of reactive metal atoms on organic surfaces can be strongly controlled by the interplay between kinetic and thermochemical factors.

Acknowledgment. We acknowledge financial support from the National Science Foundation, the Defense Advanced Research Project Agency, and the Air Force Office of Scientific Research.

Supporting Information Available: XPS data for Ti deposition (O 1s, Ti 2p, and S 2p core level spectra), Ca deposition Ca (O 1s, Ca 2p, and S 2p core level spectra), and tapping mode AFM images of SAMs before and after deposition of 25 atoms per molecule of Ti and Ca. This material is available free of charge via the Internet at http://pubs.acs.org.

References and Notes

(1) Jung, D. R.; Czanderna, A. W. *Crit. Rev. Solid State* **1994**, *19*, 1−54.

(2) Herdt, G. C.; King, D. E.; Czanderna, A. W. *Z. Phys. Chem.* **1997**, *202*, 163−196.

(3) Hooper, A.; Fisher, G. L.; Konstadinidis, K.; Jung, D.; Nguyen, H.; Opila, R.; Collins, R. W.; Winograd, N.; Allara, D. L. *J. Am. Chem. Soc.* **1999**, *121*, 8052−8064.

(4) Fisher, G. L.; Hooper, A. E.; Opila, R. L.; Allara, D. L.; Winograd, N. *J. Phys. Chem. B* **2000**, *104*, 3267−3273.

(5) Fisher, G. L.; Walker, A. V.; Hooper, A. E.; Tighe, T. B.; Bahnck, K. B.; Skriba, H. T.; Reinard, M. D.; Haynie, B. C.; Opila, R. L.; Winograd, N.; Allara, D. L. *J. Am. Chem. Soc.* **2002**, *124*, 5528−5541.

(6) Walker, A. V.; Tighe, T. B.; Reinard, M. D.; Haynie, B. C.; Allara, D. L.; Winograd, N. *Chem. Phys. Lett.* **2003**, *369*, 615−620.

(7) Walker, A. V.; Tighe, T. B.; Stapleton, J.; Haynie, B. C.; Upilli, S.; Allara, D. L.; Winograd, N. *Appl. Phys. Lett.* **2004**, *84*, 4008−4010.

(8) Walker, A. V.; Tighe, T. B.; Cabarcos, O. M.; Reinard, M. D.; Haynie, B. C.; Uppili, S.; Winograd, N.; Allara, D. L. *J. Am. Chem. Soc.* **2004**, *126*, 3954−3963.

(9) Zhou, C.; Deshpande, M. R.; Reed, M. A.; Jones, L.; Tour, J. M. *Appl. Phys. Lett.* **1997**, *71*, 611−613.

(10) Collet, J.; Vuillame, D. *Appl. Phys. Lett.* **1998**, *73*, 2681−2693.

(11) Allara, D. L.; Dunbar, T. D.; Weiss, P. S.; Bumm, L. A.; Cygan, M. T.; Tour, J. M.; Reinerth, W. A.; Yao, Y.; Kozaki, M.; Jones, L. *Ann. N.Y. Acad. Sci.* **1998**, *852*, 349−370.

(12) Collier, C. P.; Wong, E. W.; Belohradsky, M.; Raymo, F. M.; Stoddart, J. F.; Kuekes, P. J.; Williams, R. S.; Heath, J. R. *Science* **1999**, *285*, 391−394.

(13) Chen, J.; Reed, M. A.; Rawlett, A. M.; Tour, J. M. *Science* **1999**, *286*, 1550−1552.

(14) Chen, J.; Wang, W.; Reed, M. A.; Rawlett, A. M.; Price, D. W.; Tour, J. M. *Appl. Phys. Lett.* **2000**, *77*, 1224−1226.

(15) Reed, M. A.; Chen, J.; Rawlett, A. M.; Price, D. W.; Tour, J. M. *Appl. Phys. Lett.* **2001**, *78*, 3735−3737.

(16) Collier, C. P.; Mattersteig, G.; Wong, E. W.; Luo, Y.; Beverly, K.; Sampaio, J.; Raymo, F. M.; Stoddart, J. F.; Heath, J. R. *Science* **2000**, *289*, 1172−1175.

(17) Collier, C. P.; Jeppesen, J. O.; Luo, Y.; Perkins, J.; Wong, E. W.; Heath, J. R.; Stoddart, J. F. *J. Am. Chem. Soc.* **2001**, *123*, 12632−12641.

(18) Metzger, R. M.; Xu, T.; Peterson, I. R. *J. Phys. Chem. B* **2001**, *105*, 7280−7290.

(19) Chen, J.; Reed, M. A. *Chem. Phys.* **2002**, *281*, 127−145.

(20) Chang, S. C.; Li, Z. Y.; Lau, C. N.; Larade, B.; Williams, R. S. *Appl. Phys. Lett.* **2003**, *83*, 3198−3200.

(21) Vuillaume, D.; Lenfant, S. *Microelectron. Eng.* **2003**, *70*, 539−550.

(22) Lenfant, S.; Krzeminski, C.; Delerue, C.; Allan, G.; Vuillaume, D. *Nano Lett.* **2003**, *3*, 741−746.

(23) McCreery, R.; Dieringer, J.; Solak, A. O.; Snyder, B.; Nowak, A. M.; McGovern, W. R.; DuVall, S. *J. Am. Chem. Soc.* **2003**, *125*, 10748−10758. McCreery, R.; Dieringer, J.; Solak, A. O.; Snyder, B.; Nowak, A. M.; McGovern, W. R.; DuVall, S. *J. Am. Chem. Soc.* **2004**, *126*, 6200.

(24) de Boer, B.; Frank, M. M.; Chabal, Y. J.; Jiang, W. R.; Garfunkel, E.; Bao, Z. *Langmuir* **2004**, *20*, 1539−1542.

(25) Jung, G. Y.; Ganapathiappan, S.; Li, X.; Ohlberg, D. A. A.; Olynick, D. L.; Chen, Y.; Tong, W. M.; Williams, R. S. *Appl. Phys. A* **2004**, *78*, 1169−1173.

(26) McCreery, R. L. *Chem. Mater.* **2004**, *16*, 4477−4496.

(27) Stewart, D. R.; Ohlberg, D. A. A.; Beck, P. A.; Chen, Y.; Williams, R. S.; Jeppesen, J. O.; Nielsen, K. A.; Stoddart, J. F. *Nano Lett.* **2004**, *4*, 133−136.

(28) Lau, C. N.; Stewart, D. R.; Williams, R. S.; Bockrath, M. *Nano Lett.* **2004**, *4*, 569−572.

(29) Haick, H.; Ambrico, M.; Ghabboun, J.; Ligonzo, T.; Cahen, D. *Phys. Chem. Chem. Phys.* **2004**, *6*, 4538−4541.

(30) For example, see: (a) NIST Standard Reference Database, http://webbook.nist.gov, February 24, 2004. (b) *Advanced Inorganic Chemistry*; Cotton, F. A., Wilkinson, G., Murillo, C. A., Bochman, M., Eds.; Wiley-Interscience: New York, 1999; Chapters 2, 4, 6, 7, 17.

(31) For example, see: (a) Halls, J. J. M.; Walsh, C. A.; Greenham, N. C.; Marseglia, E. A.; Friend, R. H.; Moratti, S. C.; Holmes, A. B. *Nature* **1995**, *376*, 498−500. (b) Vuillaume, D.; Boulas, C.; Collet, J.; Davidovolis, J. V.; Rondelez, F. *Appl. Phys. Lett.* **1996**, *69*, 1646−1648. (c) Faraggi, E. Z.; Davidov, D.; Cohen, G.; Noach, S.; Golovsky, M.; Avny, Y.; Neumann, R.; Lewis, A. *Synth. Met.* **1997**, *85*, 1187−1190. (d) Polozonetti, G.; Russo, M. V.; Infante, G.; Furkani, A. *J. Electron Spectrosc. Relat. Phenom.* **1997**, *85*, 73−80. (e) Campbell, I. H.; Smith, D. L. *Appl. Phys. Lett.* **1999**, *74*, 561−563. (f) Bliznyuk, V.; Carter, S. A.; Scott, J. C.; Klärner, G.; Miller, R. D.; Miller, D. C. *Macromolecules* **1999**, *32*, 361−369. (g) Beierlein, T. A.; Britting, W.; Riel, H.; Haskal, E. A.; Muller, P.; Rieb, W. *Synth. Met.* **2000**, *111*−*112*, 295−297. (h) Morgado, J.; Cacialli, F.; Friend, R. H.; Chuah, B. S.; Rost, H.; Moratti, S. C.; Holmes, A. B. *Synth. Met.* **2001**, *119*, 595−596.

(32) For example, see: (a) Susac, D.; Kono, M.; Wong, K. C.; Mitchell, K. A. R. *Appl. Surf. Sci.* **2001**, *174*, 43−50. (b) Barth, S.; Müller, P.; Riel, H.; Siedler, P. F.; Riess, W.; Vestueber, H.; Bässler, H. *J. Appl. Phys.* **2001**, *89*, 3711−3719.

(33) Salaneck, W. R.; Lögdlund, M.; Birgersson, J.; Barta, P.; Lazzaroni, R.; Brédas, J. L. *Synth. Met.* **1997**, *85*, 1219−1220.

(34) Dannetun, P.; Lögdlund, M.; Frediksson, C.; Fauquet, C.; Strafström, S.; Spangler, C. W.; Brédas, J. L.; Salaneck, W. R. *J. Phys. Chem.* **1994**, *100*, 6765−6771.

(35) For example, see: (a) Dannetun, P.; Fahlman, M.; Fauquet, C.; Kajerijama, K.; Sonoda, Y.; Lazzaroni, R.; Brédas, J. L.; Salaneck, W. R. *Synth. Met.* **1994**, *67*, 133−136. (b) Lazzaroni, R.; Lögdlund, M.; Calderone, A.; Brédas, J. L.; Dannetun, P.; Fauquet, C.; Frediksson, C.; Strafström, S.; Salaneck, W. R. *Synth. Met.* **1995**, *71*, 2159−2162.

(36) Konstadinidis, K.; Taylor, A. J.; Miller, A. C.; Opila, R. L. *J. Adhes.* **1994**, *46*, 197−213.

(37) Tachibana, T.; Williams, B. E.; Glass, J. T. *Phys. Rev. B* **1992**, *45*, 11975−11981.

(38) Bodo, P.; Sundgren, J. E. *J. Vac. Sci. Technol., A* **1984**, *2*, 1498−1502.

(39) Bodo, P.; Sundgren, J. E. *J. Appl. Phys.* **1986**, *60*, 1161−1168.

(40) Ohuchi, F. S.; Freilich, S. C. *J. Vac. Sci. Technol., A* **1986**, *4*, 1039−1045.

(41) Du, M.; Opila, R. L.; Case, C. *J. Vac. Sci. Technol., A* **1998**, *16*, 155−162.

(42) Konstadinidis, K.; Zhang, P.; Opila, R. L.; Allara, D. L. *Surf. Sci.* **1995**, *338*, 300−312.

(43) Allara, D. L.; Nuzzo, R. G. *Langmuir* **1985**, *1*, 52−66.

(44) Nuzzo, R. G.; Dubois, L. H.; Allara, D. L. *J. Am. Chem. Soc.* **1990**, *112*, 558−569.

(45) Laibinis, P. E.; Whitesides, G. M.; Allara, D. L.; Tao, Y. T.; Parikh, A. N.; Nuzzo, R. G. *J. Am. Chem. Soc.* **1991**, *113*, 7152−7167.

(46) Dubois, L. H.; Nuzzo, R. G. *Annu. Rev. Phys. Chem.* **1992**, *43*, 437−463.

(47) Laibinis, P. E.; Bain, C. D.; Nuzzo, R. G.; Whitesides, G. M. *J. Phys. Chem.* **1995**, *99*, 7663−7676.

(48) Schreiber, F. *Prog. Surf. Sci.* **2000**, *65*, 151−256.

(49) Geometric factor corrections (tooling factors) for the placement of the QCM crystal relative to the sample and absolute fluxes were calibrated using AFM-measured film thicknesses at the sample and QCM crystal locations.

(50) Braun, R. M.; Blenkinsopp, P.; Mullock, S. J.; Corlett, C.; Willey, K. F.; Vickerman, J. C.; Winograd, N. *Rapid Commun. Mass Spectrom.* **1998**, *12*, 1246−1252.

(51) Tarlov, M. J.; Neuman, J. G. *Langmuir* **1992**, *8*, 1398−1405.

(52) Hagenhoff, B.; Benninghoven, A.; Spinke, J.; Liley, M.; Knoll, W. *Langmuir* **1993**, *9*, 1622−1624.

(53) Wood, M. C. Surface Characterization and Imaging with Ion-Induced Desorption and Multiphoton Resonance Ionization, Ph.D. Thesis, The Pennsylvania State University, University Park, PA, 1995.

(54) Hutt, D. A.; Cooper, E.; Leggett, G. J. *J. Phys. Chem. B.* **1998**, *102*, 174−184.

(55) Ong, T. H.; Davies, P. B.; Bain, C. D. *Langmuir* **1993**, *9*, 1836−1845.

(56) Allan, A.; McKean, D. C.; Perchard, J.-P.; Josien, M.-L. *Spectrochim. Acta* **1971**, *27A*, 1409−1437.

(57) This assignment is based on previously reported measurements in which methanol was adsorbed on both metal and metal oxide surfaces. The range of the ν_{C-O} stretch is between ∼1000 and ∼1150 cm^{-1} for M−O−CH_x, where M is the metal atom. For example, see: (a) *Infrared Spectroscopy of Adsorbed Species on the Surface of Transition Metal Oxides*;

Davidov, A. A., Ed.; John Wiley and Sons: New York, 1984. (b) Schauermann, S.; Hoffmann, J.; Johanek, V.; Hartmann, J.; Libuda, J. *Phys. Chem. Chem. Phys.* **2002**, *4*, 3909−3918. (c) Finoccio, E.; Daturi, M.; Binet, C.; Lavalley, J. C.; Blanchard, G. *Catal. Today* **1999**, *52*, 53−63.

(58) We note that the range of TO mode Ca−O stretch frequencies is reported to be 370−610 and 300−900 cm^{-1} for M−OH stretches. For example, see: *Infrared and Raman Characteristic Group Frequencies*, 3rd ed.; Socrates, G., Ed.; John Wiley and Sons: New York, 2001. In our experiments at grazing incidence on Au metal surfaces, we observe LO modes. Since the frequencies of LO modes under these conditions are shifted toward the high end of the overall absorption envelope, our spectral peaks will be shifted to higher frequencies than for the TO modes.

(59) The IR electric field screening calculations used model structures based on uniform, parallel, noninteracting isotropic layers of [Au substrate]/[organic film of ∼2 nm thickness (the model IR active oscillator represents the C−H stretching mode region of the SAM film)]/[metal overlayer of variable thickness]. The numerical calculations were based on previously developed algorithms. See: Parikh, A. N.; Allara, D. L. *J. Chem. Phys.* **1992**, *96*, 927−945. The *n* and *k* values of the complex refractive indices of the metals were taken from several sources: (a) *American Institute of Physics Handbook*, 3rd ed.; Gray, D. E., Ed.; McGraw-Hill: New York, 1972. (b) *Handbook of Optical Constants*; Palik, E. D., Ed.; Academic Press: San Diego, 1998. Since no optical constant data were available for Ca, the values for Mg were used on the basis that they are adjacent in group II and so will have similar optical properties.

(60) We note that the high-frequency shoulder of the d^- $-(CH_2)-$ antisymmetric mode diminishes in its contribution to the peak shape with increasing Ca coverage. This shoulder is typically assigned to contributions from the α-CH_2 moieties, S-CH_2, H_3OC-CH_2 (in our case), and alkyl chains with increasing conformational disorder. Although it is not possible to assign the relative contributions from the spectra, this observation suggests that Ca may react with the more disordered SAM chains. This may occur if there was a preference for the Ca atoms to react with the chains in SAM defect regions, leaving some fraction of the more ordered chains relatively intact.

(61) Attempts were not made to fit the attenuation of the Au 4f peak areas as a function of metal coverage by an overlayer growth morphology model (e.g., layer by layer vs islanding) because the chemical composition and topography (i.e., clusters vs uniform conformal deposition) of the overlayers are not known, and there is a lack of quantitative information about the mean free paths of the photoelectrons in the various possible product phases (e.g., carbides, oxides, and hydrides).

(62) Initial deposition of Ti causes a small shift to a slightly higher binding energy with a gradual return shift as coverage continues to increase. This behavior is consistent with previous reports about metal depositions on SAMs (see refs 3, 5, 7, and 42).

(63) Baer, D. R.; Marmorstein, A. M.; Williford, R. E.; Blanchard, D. L. *Surf. Sci. Spec.* **1992**, *1*, 80−86.

(64) TOF SIMS studies were carried out for both TiC and CaC_2 on Ag substrates to compare with the observed results. The titanium carbide mass spectra were found to be in good agreement. However, no comparison spectrum of calcium carbide could be obtained because CaC_2 is extremely hydroscopic and reaction with atmospheric water and oxygen could not be avoided before acquiring a TOF SIMS spectrum.

(65) *Handbook of Chemistry and Physics*, 84th ed.; Lide, D. R., Ed.; CRC Press: Boca Raton, FL, 2003; sections 12−19.